Check for updates

Bio-inspired copper complexes with Cu$_2$S cores: (solvent) effects on oxygen reduction reactions†

Jordan Mangue,[a] Iris Wehrung,[b] Jacques Pécaut,[c] Stéphane Ménage, [ID] [a] Maylis Orio [ID] *[b] and Stéphane Torelli [ID] *[a]

The need for effective alternative energy sources and "green" industrial processes is a more crucial societal topic than ever. In this context, mastering oxygen reduction reactions (ORRs) is a key step to develop fuel cells or to propose alternatives to energy-intensive setups such as the anthraquinone process for hydrogen peroxide production. Achieving this goal using bio-inspired metal complexes based on abundant and non-toxic elements could provide an environmentally friendly option. Given the prevalence of Cu-containing active sites capable of reductive activation of dioxygen in nature, the development of Cu-based catalysts for the ORR thus appears to be a relevant approach. We herein report the preparation, full characterization and (TD)DFT investigation of a new dinuclear mixed-valent copper complex **6** exhibiting a Cu$_2$S core and a bridging triflate anion. Its ORR activity was compared with that of its parent catalyst **1**. Two types of solvents were used, acetonitrile and acetone, and various catalyst/Me$_8$Fc (electron source) ratios were tested. Our results highlight a counterintuitive solvent effect for **1** and a drastic drop in the activity for **6** in coordinating acetonitrile together with the modification of its chemical structure.

Introduction

Oxygen reduction reactions (ORRs) involve the reduction of dioxygen (O$_2$) into hydrogen peroxide (O$_2$ + 2e$^-$ + 2H$^+$ → H$_2$O$_2$) and water (O$_2$ + 4e$^-$ + 4H$^+$ → 2H$_2$O).[1] On the one hand, reduction to H$_2$O takes place *via* conventional fuel cells and is an efficient method for converting chemical energy (stored in the O=O bond) into electrical energy. Unfortunately, the most powerful systems remain those that are based on noble metal-containing architectures.[2,3] On the other hand, H$_2$O$_2$ is a well-known reagent (one of the 100 most important chemicals used)[4,5] for various industrial purposes (aqueous and organic media). It is applied for water treatment,[6] paper bleaching,[7] disinfection,[8] chips making processes[9] and aerospace.[10] It is also considered the prototype of green oxidant for organic synthesis.[11] More recently, its propensity to be utilized in mono-compartmental fuel cells has emerged.[12] The consequence is an increase in the worldwide demand, which should reach 5.7 million tons by 2027.[13] More than 95% of the global H$_2$O$_2$ production comes from the so-called anthraquinone (or Riedl-Pfleiderer) process. This method is energy consuming, dangerous (use of H$_2$ and O$_2$, transportation), produces a lot of waste and requires noble-based metal (Pt or Pd) catalysts.[14] Thus, it becomes clear that providing efficient, environmentally friendly and on-site selective ORR catalysts is crucial to fulfill future needs and applications. This is particularly the case when considering the use in organic synthesis, which requires "water-free" environments.

O$_2$ activation is one of the most important processes used by nature to fulfill vital metabolic functions; thus, bio-inorganic chemists have investigated this field by means of bio-inspired or biomimetic complexes based on abundant and non-toxic transition metal ions such as Fe and Mn.[15] Mono- and dinuclear Cu-containing complexes are also reported for efficient O$_2$ activation.[16] When dealing specifically with the ORR, electron supply can be achieved *via* an electrode. Generally, H$_2$O production is mainly favored.[17–23] Extensive and deep mechanistic investigations have provided undeniable insights into the role of the solvent(s) or proton source(s) in the reactivity.[24–28] The use of sacrificial chemical electron sources such as ferrocene derivatives is an alternative. In this case, interesting results are obtained even if the activity in terms of turnover frequencies (TOFs) cannot compete with by electrocatalysis. However, H$_2$O$_2$ production can be obtained under given conditions.[23,29] In this line, we previously described the unique behavior of the dinuclear mixed valent

[a]*Univ. Grenoble Alpes, CNRS, CEA, IRIG, Laboratoire de Chimie et Biologie des Métaux, 17 rue des Martyrs, 38054 Grenoble Cedex 9, France.*
E-mail: stephane.torelli@cea.fr
[b]*Aix Marseille Univ. Centrale Med., ISM2, Marseille, France.*
E-mail: maylis.orio@univ-amu.fr
[c]*Univ. Grenoble Alpes, CEA, CNRS, IRIG, SYMMES, UMR 5819, F-38000 Grenoble, France*

†Electronic supplementary information (ESI) available: Experimental and computational details and reactivity details. CCDC 2347077 and 2347081. For ESI and crystallographic data in CIF or other electronic format see DOI: https://doi.org/10.1039/d4dt01629g
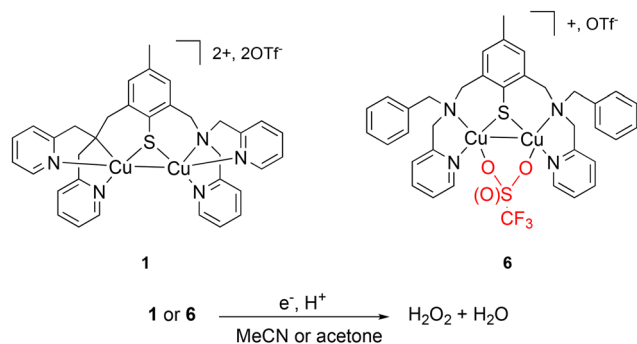
Fig. 1 Chemical representations of **1**,[30] **6** and the targeted ORR.

(MV) complex **1** (Fig. 1),[30] which proves to be selective either for H_2O_2 or H_2O depending on the amount of octamethyl or decamethylferrocene (Me_8Fc or $Me_{10}Fc$) present in the medium (acetonitrile). In all cases, reactions are extremely fast when dealing with homogeneous catalysis (TOF ~10 s^{-1}), with the full consumption of the ferrocene derivative.[31]

Driven by the hypothesis that the unique reactivity of **1** could be related to its N_3S environment and the presence of the Cu–Cu bond, we prepared a new MV copper complex having a N_2S motif. This will open the Cu coordination sphere (s) to exogenous ligand(s) such as counter-anions and/or solvent molecules. Consequently, complex **6** featuring a ligated OTf$^-$ (OTf$^-$ = trifluoromethanesulfonate anion) was isolated and fully characterized. The structural differences between **1** and **6** finally allowed to investigate their abilities for ORR either in non-coordinating acetone or in coordinating acetonitrile (Fig. 1). The results of this work clearly demonstrate the influence of the Cu environment on the reactivity in terms of selectivity, kinetics and solvent tolerance of the reaction.

Results and discussion

Preparation and characterization of 6

The synthesis of the **(BAMP)$_2$$^{S–S}$** ligand (Fig. 2 and ESI† for experimental details) slightly differs from the ones we already reported for the preparation of other disulfide-containing derivatives.[30,32] This time, the deprotection of the key methyl-diformyl-S-thiocarbamate precursor (**I**) was achieved under
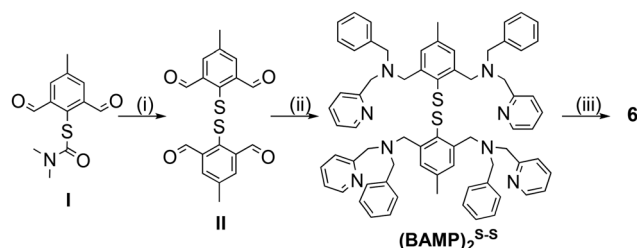

Fig. 2 Preparation of the (BAMP)$_2$$^{S–S}$ ligand from (**I**)[30] and metalation into **6**.

mild conditions (1 M NaOH instead of LiAlH$_4$ or concentrated KOH and heating), and dimerization into the disulfide was performed using iodine. Subsequent reductive amination with [(benzyl-amino)methyl]pyridine and sodium triacetoxyborohydride finally gave the title ligand. Metalation with four molar eq. of [Cu(CH$_3$CN)$_4$](OTf) in acetone resulted in the isolation of **6** as a dark purple solid.

The ESI-MS of **6** in acetone (Fig. S1, ESI†) displays isotopic patterns at m/z = 671.1, 820.0 and 968.9 corresponding to mono-charged ions ([BAMP^S + 2Cu]$^+$, [BAMP^S + 2Cu + 1OTf]$^+$, and [BAMP^S + 2Cu + 2OTf]$^+$, respectively) that attest to the presence of the Cu$_2$S core as well as the integrity of the ligand. Crystals suitable for X-ray analysis were obtained upon layering pentane upon an acetone solution of the complex. As already observed for other members of the series,[30,32,33] the reductive cleavage of the S–S bond occurs and leads to the formation of a MV(II,I) dinuclear species (Fig. 3). Both metal centers are pentacoordinated by the N/S atoms from the ligand, an O-atom from a triflate anion and the neighboring Cu. The Cu1–O1S2 = 2.176 (2) Å and Cu2–O2S2 = 2.674 (9) Å bond distances clearly indicate a weak bridging interaction. A Cu–Cu bond of 2.5475(5) Å length is present and will be further confirmed by theoretical calculations. When comparing **6** with **1** and focusing on the Cu$_2$S core, the metrics are relatively close with Cu1–Cu2 = 2.5762(12), Cu1–S = 2.177(2) and Cu2–S = 2.193(2) for the latter.

Density functional theory (DFT) calculations were then performed to investigate the structure and properties of **6** and support the experimental findings. The complex was first subjected to geometry optimization in implicit solvent for comparison with the solid-state structure (Fig. 4). The main result is that the integrity of the structure is retained. The computed Cu1–S1, Cu2–S1, Cu1–N1, Cu1–N2, Cu2–N3 and Cu2–N4 bond distances of 2.211, 2.207, 2.133, 1.986, 2.140 and 1.983 Å indeed fall in the range of the experimental ones. Looking more specifically at the Cu1–Cu2 motif, a deviation between
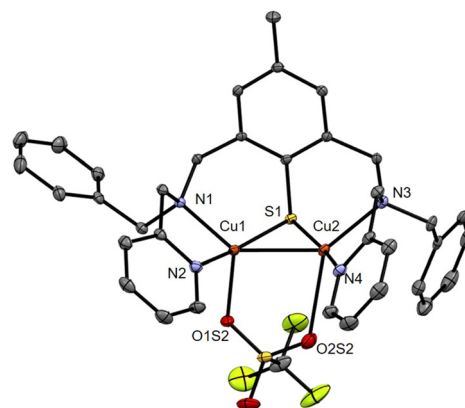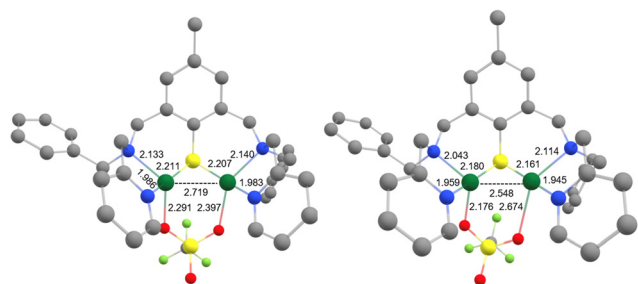

Fig. 3 ORTEP diagram (30% probability) for the dicationic unit of **6**. H-atoms are omitted for clarity. Selected bond distances (Å): Cu1–Cu2 2.5475(5), Cu1–S1 2.1798(8), Cu2–S1 2.1661(8), Cu1–N1 2.043(2), Cu1–N2 1.959(3), Cu1–O1S2 2.176(2), Cu2–N3 2.114(3), Cu2–N4 1.945(3), Cu2–O2S2 2.674(9); see Tables S1–S3, ESI.†
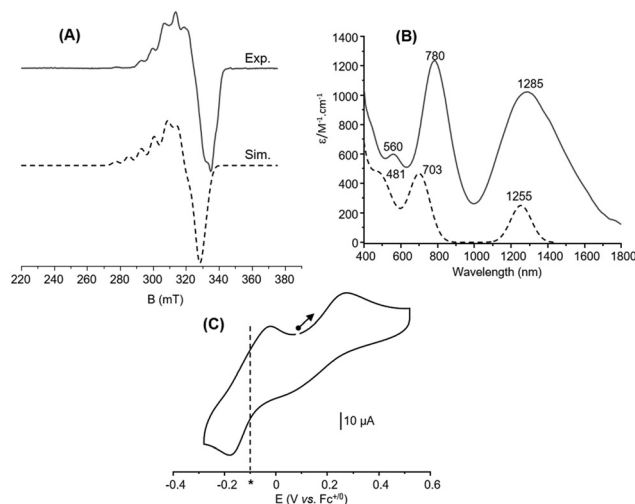
Fig. 4 Comparison of the DFT-optimized geometry of **6** (left) and X-ray solid-state structure (right). H-atoms are omitted for clarity. Color scheme: Cu olive green, S yellow, O red, N dark blue, F light green, C light grey.

Fig. 5 Characterization of **6** in acetone: (A) experimental (solid line, 10 K, 0.67 mM with microwave freq. 9.40 GHz; power 0.25 mW; mod. ampl. 1 mT; freq. 100 kHz) and Easyspin-simulated (dashed line) X-band EPR spectra. (B) Experimental (solid line) and TD-DFT-calculated (dashed line) UV-vis/NIR spectra. (C) Cyclic voltammogram (0.7 mM) in acetone with 0.1 M TBAPF$_6$ as the supporting electrolyte and glassy carbon as the working electrode. The curve corresponds to the initial scan at 100 mV s^{-1} starting from the open-circuit potential and (*) indicates the standard potential obtained through DFT calculations.

the computed (2.719 Å) and the experimental (2.5475(5) Å) metal–metal bond distance is observed. Finally, a significant shortening of one of the two Cu–OTf bonds (from 2.674(9) to 2.397 Å) was obtained, which somehow rendered the binding mode of the OTf anion more symmetrical. This can be tentatively attributed to the relaxation of the complex upon geometry optimization in the solvated medium, as opposed to the frozen X-ray (solid-state) structure. This finding suggests that particular attention will have to be paid when conducting the computational modeling since it may have repercussions on the calculated (UV-Vis/NIR, EPR and redox) properties.

Insights into the Cu–Cu bond is obtained by Natural Bond Order (NBO) analysis using the DFT-optimized structure of **6** (Fig. S2 and Table S4, ESI†). The calculated Wiberg bond index of 0.54 compares quite well with the one obtained for **1** (0.40), thus supporting the presence of a metal–metal bond. The relevant occupied natural orbital representing this Cu–Cu motif corresponds to a σ (4p 3d/4p 3d) overlap between the two metal centers. Note that a similar orbital was also found from calculations using the X-ray crystal structure, featuring a shorter Cu–Cu distance of 2.5475(5) Å (Fig. S3 and Table S4, ESI†). Electronic structure calculations using the DFT-optimized structure of **6** provide a singly occupied molecular orbital (SOMO) that is predominantly metal-based and features 30, 27 and 20% contributions from the Cu1, Cu2 and S centers, respectively (Fig. S4, ESI†). Mulliken population analysis (Fig. S4 and Table S5, ESI†) shows that the spin density is equally distributed between the two copper centers and the coordinating sulfur, which strongly suggests that **6** is a fully delocalized (Cu$^{1.5}$Cu$^{1.5}$) MV species.

The electronic properties of **6** were then investigated in acetone. The X-band EPR spectrum recorded at 10 K (Fig. 5(A)) exhibits a complicated multiline pattern, as already observed for **1** and attributed to a (Cu$^{1.5}$Cu$^{1.5}$) MV state. This is further confirmed since the simulated spectrum (Fig. 5(A)) using the computed parameters obtained with the DFT-optimized structure with a fully delocalized valence (Table S6, ESI†) adequately reproduces the main experimental features. In the same vein, the UV-Vis/NIR absorption spectrum (Fig. 5(B)) displays intense and well-defined absorption bands resembling those of **1** in acetone. The near-infrared feature at 1285 nm (ε = 1025

M^{-1} cm^{-1}) is thus assigned to an intervalence charge transfer transition (IVCT) and the others at 780 nm (ε = 1245 M^{-1} cm^{-1}) and 560 nm (ε = 605 M^{-1} cm^{-1}) to ligand-to-metal charge transfer (LMCT) transitions. These attributions are corroborated by TD-DFT calculations since three main absorption bands at 481 nm, 703 nm and 1255 nm are indeed obtained (Fig. 5(B), Fig. S5 and Table S7, ESI†).

Interestingly, the TD-DFT-computed UV-Vis/NIR spectrum using the X-ray crystal structure (Fig. S6 and Table S8, ESI†) exhibits two main absorption bands at 1007 nm and 613 nm. Although far from the experimental values, these signatures are, however, similar to those obtained when recording the solid-state spectrum of **6** diluted in BaSO$_4$ (Fig. S6, ESI†) with bands at 1005 nm and 605 nm. This result reinforces the finding that solvation has repercussions on the electronic structure of the complex once solubilized.

Finally, the CV curve displays two distinct redox processes (Fig. 5(C)) when starting at the open-circuit potential (OCP) towards the anodic direction. The first one at E_{pa} = 0.27 V vs. Fc$^{+/0}$ is irreversible and attributed to Cu^{II}Cu^{I} → Cu^{II}Cu^{II}. The second one observed at −0.10 V vs. Fc$^{+/0}$ (E_{pa} = −0.02 V, E_{pc} = −0.18 V, ΔE_p = 0.16 V) is quasi reversible and corresponds to Cu^{II}Cu^{I} → Cu^{I}Cu^{I}. DFT calculations (optimized structure) provide a computed redox potential of −0.102 V vs. Fc$^{+/0}$ for the cathodic region that matches the experimental data (Tables S9 and S10, ESI†) and support the above assignment. The irreversibility of the anodic part clearly indicates structural changes at the metal coordination sphere(s) that stabilizes the *in situ* generated dicopper(II) state. No noticeable changes

occur on the reversibility when performing a CV scan towards the cathodic direction from the OCP (Fig. S7, ESI†) One can note that a reversible oxidation process was on the contrary evidenced for **1**.

Altogether, this set of experimental and theoretical data is in favor of the structure of **6** being retained in acetone. What also emerges and needs to be emphasized is that the DFT-optimized structure is here perfectly adapted to describe the conformation and the electronic properties of **6** in solution.

Catalytic O_2 reduction by 1 and 6 with Me_8Fc and lutidinium tetrafluoroborate (LutH)

We already showed that **1** is capable of ORR in coordinating MeCN, its structure being maintained in this solvent as it is in non-coordinating acetone.[31] Selectivity (H_2O_2 *vs.* H_2O) is achieved by controlling the relative excess of the sacrificial electron source (Me_8Fc) compared to the Cu catalyst in the presence of lutidinium tetrafluoroborate (LutH) as the chemically innocent proton source. With **6** in hand and its coordination sphere slightly different from that of **1**, comparing the ORR abilities of both catalysts in MeCN or acetone could provide insights into the parameters at stake for orienting the selectivity. The experimental conditions are the same as those already used for **1** in MeCN. First, the ORR activity of **1** in acetone was investigated. The results (Table 1 and Table S11, ESI†) indicate, as already observed in MeCN, that Me_8Fc is entirely consumed for each condition since the expected absorbance values for full Me_8Fc^+ accumulation at $\lambda_{maxMe8Fc+}$ = 750 nm (ε = 460 M^{-1} cm^{-1} in acetone) are experimentally obtained (Fig. 6(A) and Fig. S8(A)–S10, ESI†). Interestingly, the kinetics are longer compared to those previously determined in MeCN. Considering that coordinating solvents such as MeCN usually slow down the reactivity, this quite counterintuitive result could indicate that no labile position(s) are available for MeCN at the metal coordination sphere(s) during catalysis.

In large Me_8Fc excess, a model with two k_{obs} values is required, suggesting chemical changes at the catalyst with time in the reaction mixture that also contains accumulated O_2-reduced species. Second, the ORR activity of **6** was studied in MeCN ($\lambda_{maxMe8Fc+}$ = 750 nm, ε = 390 M^{-1} cm^{-1}) and acetone (Fig. 6(B) and (C)). In acetone, full Me_8Fc consumption also occurs (Table 1, Fig. S8(B), S11–12 and Table S11, ESI†). The reaction rates and times are roughly independent of $[Me_8Fc]$. An average value of 14 s is calculated that makes **6** slower than **1** at low Me_8Fc concentrations (*i.e.*, from 1/10/400 to 1/40/400, Cat/Me_8Fc/LutH, Table S11, ESI†) but more efficient at high Me_8Fc concentrations (*i.e.*, from 1/60/400, Cat/Me_8Fc/LutH, Table S11, ESI†). A drastic change is observed in MeCN (Table 1, Fig. S8(C), S13–S14 and Table S11, ESI†); though the reaction is complete up to 40 molar eq. of Me_8Fc within a longer but still acceptable timescale, very slow kinetics are obtained from 60 molar eq. to 100 molar eq. In these cases, the TON_{max} values are not even reach after 6000 s. This time, all the kinetic traces clearly indicate two different regimes: a "fast" one and a second slower one, suggesting that the catalyst evolves during the reaction towards a less reactive species (slow poisoning). One can also note that a factor of 10 for the reaction time is obtained between 20 molar eq. and 40 molar eq. Considering all these kinetic data, one might also note a rather unexpected trend for the k_{obs} values for **1** that decrease when increasing the amount of Me_8Fc. This negative order has to be opposed to the zero-order obtained for **6** in acetone (reactivity independent of $[Me_8Fc]$). The former may correlate with a less efficient outer sphere electron transfer (steric hindrance at the metal centre(s)) that retard the reactivity, as already invoked for the dinuclear Mn species.[34] Then, the selectivity of both complexes was evaluated *via* H_2O_2 titration (Tables S1 and S11, ESI†) with a dedicated Ti-based porphyrin (Fig. S15, ESI†).[35,36] In acetone, **1** mainly produced H_2O_2 when using low Me_8Fc loadings, as already observed in MeCN. In acetone, **6** is rather unselective at low $[Me_8Fc]$ compared to **1**, as it is the case when switching to MeCN (34% maximum). For both

Table 1 Selected ORR experiments performed with **1** and **6** in air-saturated acetone or MeCN at room temperature using Me_8Fc and $LutHBF_4$ as the electron and proton sources, respectively. The values obtained for **1** in MeCN (already reported)[31] are listed for comparison. See the ESI for experimental details and Table S11† for full data

Entry	$[Me_8Fc]$ (mM)	Cat/e^-/H^+	TON	TON_{max}	k_{obs} (s^{-1})	t (s)	% H_2O_2 Me_8Fc	% H_2O Me_8Fc	TOF^b (s^{-1})
1 in MeCN[31]	0.5	1/10/400	10	10	1.06 ± 0.02	4.1 ± 0.2	90	10	5.3 ± 0.3
	3.0	1/60/400	60	60	0.13 ± 0.01	28.1 ± 0.5	51	49	8.3 ± 0.3
	5.0	1/100/400	100	100	0.12 ± 0.01	41.2 ± 2	10	90	14.1 ± 0.4
1 in acetone	0.5	1/10/400	10	10	0.30 ± 0.05	22.0 ± 0.8	70	30	1.5 ± 0.2
	3.0	1/60/400	60	60	0.05 ± 0.004	91 ± 4	31	69	1.9 ± 0.2
	5.0	1/100/400	100	100	0.10 ± 0.02 0.014 ± 0.009	268 ± 10	20	80	2.7 ± 0.4
6 in acetone	0.5	1/10/400	10	10	0.51 ± 0.01	11.2 ± 0.9	42	54	3.1 ± 0.2
	3.0	1/60/400	60	60	0.40 ± 0.004	15.1 ± 1.2	11	89	10.6 ± 0.4
	5.0	1/100/400	100	100	0.46 ± 0.006	15.5 ± 1.3	5	95	17.6 ± 0.2
6 in MeCN	0.5	1/10/400	10	10	0.51 ± 0.05 89.9 ± 8	340 ± 30	34	66	<1
	3.0	1/60/400	50^a	60	nd	>6000	nd	nd	nd
	5.0	1/100/400	40^a	100	nd	>6000	nd	nd	nd

^{a} After 6000 s reaction time; nd: not determined. ^{b} Determined for the first kinetic event in the case of multi regimes.
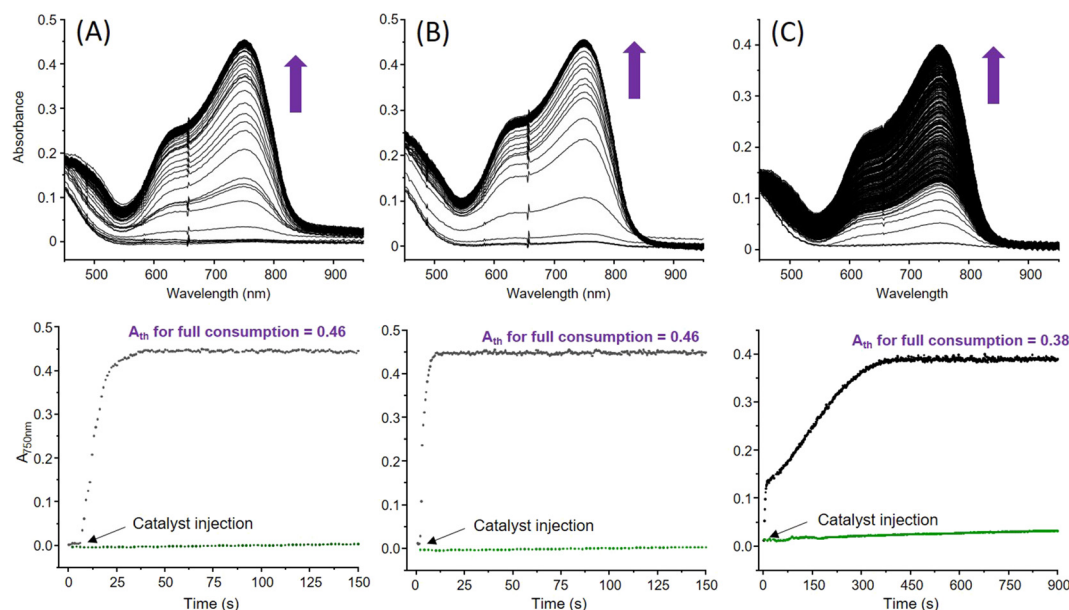
Fig. 6 Selected UV-vis absorption spectral changes and time dependence recorded at 785 nm corresponding to the accumulation of Me$_8$Fc$^+$ during the ORR performed in saturated O$_2$-solutions using Cu catalysts (0.05 mM), Me$_8$Fc (2 mM) and LutH (20 mM) corresponding to 1/20/ 400 molar eq. for **1** in acetone (A), **6** in acetone (B) and **6** in MeCN (C) at 298 K. The black arrows indicate the injection of the catalyst in the reaction mixture containing pre-incubated Me$_8$Fc and LutH. In each case, the blank experiment using commercial [Cu(CH$_3$CN)$_4$](OTf) is shown with the green trace.

complexes, H$_2$O remains the main product for large Me$_8$Fc excess. Finally, looking at the TOFs, values between 1.5 s^{-1} and 17.6 s^{-1} are obtained at best. This result is rather modest compared to the huge efficiency usually obtained under homogeneous electrocatalytic conditions for the reported copper complexes[25,28,37–40] and in the same range as those reported by Fukuzumi with stopped-flow experiments for the study of the well-known mononuclear [(tmpa)(Cu^{II})](ClO$_4$)$_2$ species.[17]

The behavior observed for **6** in MeCN urged us to probe its chemical structure in this solvent for comparison with acetone. Noticeable changes occur on the UV-Vis/NIR and EPR spectra as well as on the CV curve (Fig. 7). The well-defined and intense absorption bands observed in acetone gave way to a featureless spectrum with no band in the NIR region, which suggests a change in the valence state from mixed to localized (Fig. 7(A)). This is in line with the EPR spectrum that becomes characteristic of a mononuclear Cu(II) complex with axial symmetry (four lines pattern; $I_{Cu} = 3/2$, $2nI + 1 = 4$ with $n = 1$, Fig. 7 (B)). Finally, even if the CV (Fig. 7(C)) curve resembles the one recorded in acetone, a non-negligible cathodic shift occurs for the Cu^{II}Cu^{I} → Cu^{I}Cu^{I} process from −0.10 V to −0.22 V vs. Fc$^{+/0}$ (E_{pa} = −0.18 V, E_{pc} = −0.26 V, ΔE_p = 0.08 V) and a slight one (0.05 V) is detected for Cu^{II}Cu^{I} → Cu^{II}Cu^{II} (from E_{pa} = 0.27 V vs. Fc$^{+/0}$ to E_{pa} = 0.22) that remains irreversible. The important result here is that the Cu^{II}Cu^{I} → Cu^{I}Cu^{I} event remains accessible by Me$_8$Fc to perform ORR. As observed in acetone, a similar CV curve is obtained when scanning towards the cathodic region (Fig. S16, ESI†). Additionally, the smaller ΔE_p in MeCN (70 mV to 90 mV) compared to that observed in acetone
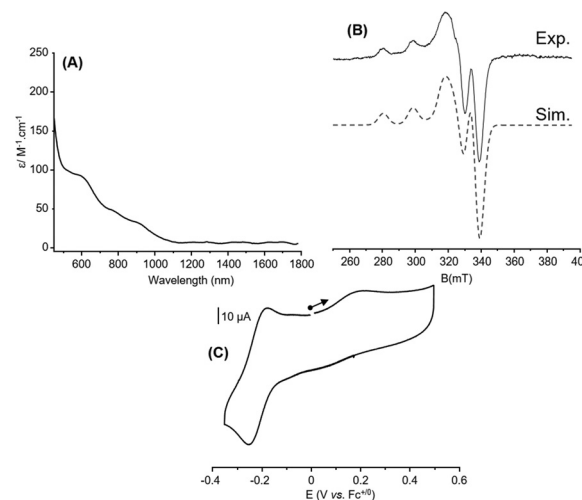
Fig. 7 Characterization of **6** in MeCN: (A) UV-vis/NIR and (B) X-band EPR spectra (solid line, 10 K, 0.5 mM with microwave freq. 9.41 GHz; power 0.25 mW; mod. ampl. 1 mT; freq. 100 kHz) and SimFonia simulation (dashed line) with g_1 = 2.041, g_2 = 2.043, g_3 = 2.18, A_1 = 57 MHz, A_2 = 86 MHz and A_3 = 550 MHz; (C) CV (0.6 mM) in MeCN with 0.1 M TBAPF$_6$ as the supporting electrolyte and glassy carbon as the working electrode. The curve corresponds to the initial scan at 100 mV s^{-1} starting from the open-circuit potential.

(130 mV to 180 mV) for this scan rate-dependent redox event (Fig. S15 in the ESI†) also points out different electron transfer efficiencies, which could have consequences on the activity.

Electron self-exchange rate constants for **6** in both solvents were consequently determined by means of CV experiments (Fig. S17 and S18, ESI†). k_{el} values of $1.5(1) \times 10^{-3}$ cm s^{-1} and $1.1(1) \times 10^{-2}$ cm s^{-1} (or estimated as $k_{hom} = 2.3(2) \times 10^5$ L mol^{-1} s^{-1} and $1.67(6) \times 10^6$ L mol^{-1} s^{-1}) were obtained in acetone and MeCN, respectively, indicating a faster electron transfer in MeCN, consistent with the ΔE_p values. This result also suggests that this parameter is not directly related to the trend observed for ORR and the k_{obs} values. Given these preliminary data, it is clear that **6** exists at different valence states/chemical structures when solvated in acetone or MeCN. These changes have sufficient repercussions on the nature of the coordination sphere and the electronics so that the ORR activity is affected in terms of kinetics and/or selectivity. Indeed, for the 1/40/400 condition, **6** turns to be 250 times faster in acetone compared to MeCN (13.8 s *vs.* 3500 s for full Me$_8$Fc consumption, Table S11 in the ESI†).

Conclusion

To conclude, we report here the preparation, full characterization and ORR activity of a new MV dicopper complex **6** that is compared to its parent catalyst **1**. Both complexes contain a Cu$_2$S MV core but differ by the number of coordinating atoms from the ligands. In the case of **6**, this leads to the presence of potentially exchangeable position(s). Theoretical investigations demonstrate in detail that special attention must be paid to the use of an optimized *vs.* X-ray structure to probe the electronic properties. In our case, the former is more suitable. From a reactivity point of view, significant differences in the kinetics and selectivity for ORR (k_{obs} and reaction times) are obtained. **1** remains the most selective catalyst since the control of the amount of the sacrificial electron source allows to swing from H$_2$O$_2$ to H$_2$O as the main product. **6** does not exhibit such a pronounced selectivity but appears to be the fastest in acetone. Comparatively, its reactivity in MeCN is rather poor. Interestingly, the data also suggest different reaction orders in Me$_8$Fc depending on the catalyst. We tentatively correlate this output with differences in the outer sphere electron transfer efficiencies linked to the steric hindrance around the metal ions either during the Cu^{II}Cu^{II} reduction or for the reduction of the corresponding O$_2$-adducts. Work including the determination of the rate-limiting step is currently under progress to clarify this point as we also continue to study in detail the structural changes resulting from the solvation of **6** in MeCN in order to understand its inefficiency for ORR. Post-catalysis verification that the catalyst(s) are still intact still needs to be optimized since analysis on the crude mixtures are plagued by the presence of Me$_8$Fc$^+$, LutH and Lut in large excess that preclude any unambiguous EPR, CV or NMR studies. This may lead to new architectures and exploration of the ORR activity of such Cu$_2$S cores through the prism of the structure–activity relationship that undoubtedly correlates with the fate of the Cu$_2$/O$_2$ adduct(s) intermediates formed in the reaction medium.

Author contributions

Stéphane Torelli and Maylis Orio designed this research and wrote the paper. Jordan Mangue, Jacques Pécaut and Stéphane Torelli performed all the syntheses, characterizations and catalytic studies. Iris Wehrung and Maylis Orio conducted the theoretical calculations. Stephane Torelli, Maylis Orio and Stéphane Ménage discussed this work. All authors have given approval to the final version of the manuscript.

Data availability

The data supporting this article have been included as part of the ESI.†

Crystallographic data for **6** and **II** have been deposited at the CCDC under 2347081 and 2347077.†

Conflicts of interest

There are no conflicts to declare.

References

1 M. L. Pegis, C. F. Wise, D. J. Martin and J. M. Mayer, *Chem. Rev.*, 2018, **118**, 2340–2391.
2 X. Wang, Z. Li, Y. Qu, T. Yuan, W. Wang, Y. Wu and Y. Li, *Chem*, 2019, **5**, 1486–1511.
3 J. Zhao, C. Fu, K. Ye, Z. Liang, F. Jiang, S. Shen, X. Zhao, L. Ma, Z. Shadike, X. Wang, J. Zhang and K. Jiang, *Nat. Commun.*, 2022, **13**, 685.
4 R. L. Myers, *The most 100 Most Important Chemical Compounds*, Greenwood Press, London, 2007.
5 J. M. Campos-Martin, G. Blanco-Brieva and J. L. G. Fierro, *Angew. Chem., Int. Ed.*, 2006, **45**, 6962–6984.
6 C. Chu, Z. Chen, D. Yao, X. Liu, M. Cai and S. Mao, *Angew. Chem., Int. Ed.*, 2024, **63**, e202317214.
7 A. Walawska, M. Olak-Kucharczyk, A. Kaczmarek and M. H. Kudzin, *Materials*, 2024, **17**, 1355.
8 A. Ayub, Y. K. Cheong, J. C. Castro, O. Cumberlege and A. Chrysanthou, *Bioengineering*, 2024, **11**, 205.
9 M. McKoy, *C&EN*, 2017, **95**(40), 32–33.
10 L. Wang, J. Zhang, Y. Zhang, H. Yu, Y. Qu and J. Yu, *Small*, 2022, **18**, e2104561.
11 E. T. Poursaitidis, P. L. Gkizis, I. Triandafillidi and C. G. Kokotos, *Chem. Sci.*, 2024, **15**, 1177–1203.
12 S. Jeon, H. An and Y. Chung, *Sustainable Energy Fuels*, 2022, **6**, 841–850.

13 M. Melchionna and P. Fornasiero, *Chem*, 2019, **5**, 1927–1928.

14 R. Ciriminna and L. Albanese, *ChemSusChem*, 2016, **9**, 3374–3381.

15 T. Devi, Y.-M. Lee, W. Nam and S. Fukuzumi, *Coord. Chem. Rev.*, 2020, **410**, 213219.

16 C. E. Elwell, N. L. Gagnon, B. D. Neisen, D. Dhar, A. D. Spaeth, G. M. Yee and W. B. Tolman, *Chem. Rev.*, 2017, **117**, 2059–2107.

17 S. Fukuzumi, H. Kotani, H. R. Lucas, K. Doi, T. Suenobu, R. L. Peterson and K. D. Karlin, *J. Am. Chem. Soc.*, 2010, **132**, 6874.

18 S. Kakuda, R. L. Peterson, K. Ohkubo, K. D. Karlin and S. Fukuzumi, *J. Am. Chem. Soc.*, 2013, **135**, 6513.

19 M. Langerman and D. G. H. Hetterscheid, *Angew. Chem., Int. Ed.*, 2019, **58**, 12974–12978.

20 H. Kotani, T. Yagi, T. Ishizuka and T. Kojima, *Chem. Commun.*, 2015, **51**, 13385–13388.

21 S. N. Chowdhury, S. Biswas, P. Das, S. Paul and A. N. Biswas, *Inorg. Chem.*, 2020, **59**, 14012–14022.

22 S. Kakuda, C. J. Rolle, K. Ohkubo, M. A. Siegler, K. D. Karlin and S. Fukuzumi, *J. Am. Chem. Soc.*, 2015, **137**, 3330–3337.

23 D. Das, Y.-M. Lee, K. Ohkubo, W. Nam, K. D. Karlin and S. Fukuzumi, *J. Am. Chem. Soc.*, 2013, **135**, 2825–2834.

24 S. N. Chowdhury, S. Biswas, S. Das and A. N. Biswas, *Dalton Trans.*, 2023, **52**, 11581–11590.

25 M. Langerman, M. van Dorth and D. G. H. Hetterscheid, *Eur. J. Inorg. Chem.*, 2023, **26**, e202300218.

26 N. W. G. Smits, D. Rademaker, A. I. Konovalov, M. A. Siegler and D. G. H. Hetterscheid, *Dalton Trans.*, 2022, **51**, 1206–1215.

27 S. D'Agostini, K. G. Kottrup, C. Casadevall, I. Gamba, V. Dantignana, A. Bucci, M. Costas, J. Lloret-Fillol and D. G. H. Hetterscheid, *ACS Catal.*, 2021, **11**, 2583–2595.

28 N. W. G. Smits, B. van Dijk, I. de Bruin, S. L. T. Groeneveld, M. A. Siegler and D. G. H. Hetterscheid, *Inorg. Chem.*, 2020, **59**, 16398–16409.

29 S. Fukuzumi, L. Tahsini, Y.-M. Lee, K. Ohkubo, W. Nam and K. D. Karlin, *J. Am. Chem. Soc.*, 2012, **134**, 7025–7035.

30 S. Torelli, M. Orio, J. Pécaut, H. Jamet, L. Le Pape and S. Ménage, *Angew. Chem., Int. Ed.*, 2010, **49**, 8249–8252.

31 J. Mangue, C. Gondre, J. Pécaut, C. Duboc, S. Ménage and S. Torelli, *Chem. Commun.*, 2020, **56**, 9636–9639.

32 C. Esmieu, M. Orio, S. Torelli, L. Le Pape, J. Pecaut, C. Lebrun and S. Menage, *Chem. Sci.*, 2014, **5**, 4774–4784.

33 C. Esmieu, M. Orio, J. Mangue, J. Pecaut, S. Menage and S. Torelli, *Chem. – Eur. J.*, 2018, **24**, 5060–5063.

34 M. Gennari, D. Brazzolotto, J. Pécaut, M. V. Cherrier, C. J. Pollock, S. DeBeer, M. Retegan, D. A. Pantazis, F. Neese, M. Rouzières, R. Clérac and C. Duboc, *J. Am. Chem. Soc.*, 2015, **137**, 8644–8653.

35 C. Matsubara, N. Kawamoto and K. Takamura, *Analyst*, 1992, **117**, 1781–1784.

36 K. Takamura, C. Matsubara and T. Matsumoto, *Anal. Sci.*, 2008, **24**, 401–404.

37 M. L. Skavenborg, M. S. Møller, C. J. Miller, J. Hjelm, T. D. Waite and C. J. McKenzie, *Inorg. Chem.*, 2023, **62**, 18219–18227.

38 C. J. M. van der Ham, D. N. H. Zwagerman, L. Wu, J. P. Hofmann and D. G. H. Hetterscheid, *ChemElectroChem*, 2022, **9**, e202101365.

39 B. van Dijk, J. P. Hofmann and D. G. H. Hetterscheid, *Phys. Chem. Chem. Phys.*, 2018, **20**, 19625–19634.

40 M. L. Pegis, B. A. McKeown, N. Kumar, K. Lang, D. J. Wasylenko, X. P. Zhang, S. Raugei and J. M. Mayer, *ACS Cent. Sci.*, 2016, **2**, 850–856.